3D Morphology of Bimodal Porous Copper with Nano-Sized and Micron-Sized Pores to Enhance Transport Properties for Functional Applications

Lijie Zou ^{a, b}, Mingyuan Ge ^c, Jianming Bai ^c, Chonghang Zhao ^b, Hao Wang ^a,

Xianghui Xiao^c, Hui Zhong ^d, Sanjit Ghose ^c, Wah-Keat Lee^c,

Qiang Shen ^{a*}, Fei Chen ^{a*}, Yu-chen Karen Chen-Wiegart ^{b, c*}

Abstract:

Multiscale porous metals with multiscale porosity from nanometer to micrometer have high specific surface area and high effective diffusivity for ion transport, thereby enhancing functionalities and extending the applications of porous metals. In this study, Cu-Fe-Al ternary system was selected as the precursor alloy to construct multiscale, bimodal porous copper by chemical dealloying method. The effect of phase composition and initial microstructure of precursor alloys (Al_xFe_{75-x}Cu₂₅, x=10-60) on the three dimensional (3D) morphology of multiscale porous metals were systematically investigated, with a goal to precisely control the multiscale porous structure. The four crystal structure phases (BCC, FCC, B2 and monoclinic) in precursor alloys were analyzed by synchrotron X-ray diffraction refinement. The 3D morphology, feature size distribution and tortuosity of four representative porous Cu after dealloying Al_xFe_{75-x}Cu₂₅ (x= 10, 30, 50 and 60) precursor alloys were directly visualized and quantified via advanced synchrotron X-ray nano-tomography. The relationship between the phases / crystal structures of precursor alloys and their corresponding porous morphology was established: the micron-sized pores in bimodal porous Cu are formed by dissolving of CuFeAl phase with BCC and monoclinic crystal structures, and the nano-sized pores are formed by dealloying of CuFeAl phase with FCC and B2 crystal structures. The size of nanoporous structure depends on the ratio between the more noble vs. more active components in the precursor alloy, while the size of microporous structure depends on the corresponding phase size in precursor alloy. The tortuosity

^a State Key Lab of Advanced Technology for Materials Synthesis and Processing, Wuhan University of Technology, Wuhan 430070, China

^b Department of Materials Science and Chemical Engineering, Stony Brook University, Stony Brook, New York 11794, United States

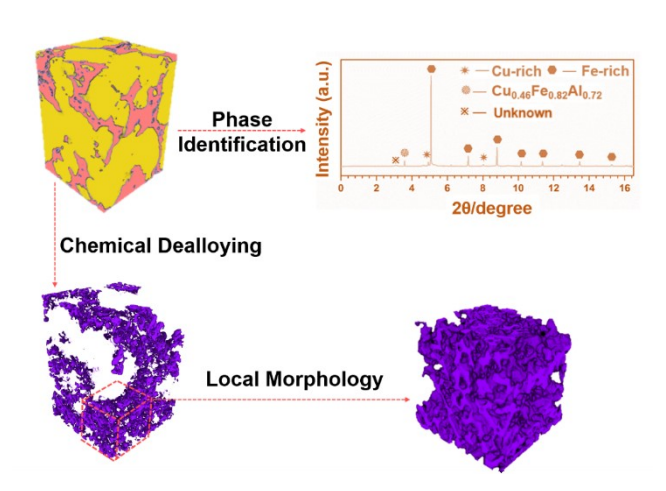
^c National Synchrotron Light Source - II, Brookhaven National Laboratory, Upton, New York 11973, United States

^d Department of Joint Photon Science Institute, Stony Brook University, Stony Brook, New York 11794, United States

^{*}corresponding authors: Karen.Chen-Wiegart@stonybrook.edu; chenfei027@whut.edu.cn; sqqf@whut.edu.cn

results showed that the multiscale porous structure with both nanoporosity and microporosity exhibits lower tortuosity, which will enhance transport properties for functional applications.

TOC



Key words: nano-CT, X-ray diffraction, nanoporous, TXM, transmission X-ray microscopy

1. Introduction

Multiscale porous metals, with their porous size spanning from nanometers to micrometers, possess unique properties: the high specific surface area enabled by nanoporous structure provides chemical and physical functionalities ^{1 2 3}; simultaneously, the larger microporous structure provides excellent transport properties for long range ions diffusion ⁴. Therefore, multiscale porous metals have a wide range of functional applications including electrochemical sensors ⁵, heat exchangers ⁶, catalysts ⁷, and energy storage ^{8 9 10}. Multiscale porous metals can be fabricated via sintering, additive manufacturing (AM), templating and dealloying methods ^{11 12 13 14}. Specifically, dealloying is a versatile method to fabricate multiscale bicontinuous multiscale porous metals.

Dealloying method, involving selective dissolution of more active alloy component(s) and the self-rearrangement of the remaining elements, has attracted great attention and been utilized to fabricate a sponge-like, highly interconnected porous structure for functional applications. Dealloying

method can be categorized according to different dealloying agents and conditions used to dealloy the precursor alloys: chemical dealloying ^{1 15}, electrochemical dealloying ^{16 17}, solid-state interfacial dealloying ^{13 18}, liquid metal dealloying ^{19 20}, and vapor phase dealloying ^{21 22}; each method possesses unique characteristics and applications. In particular, chemical dealloying method is an effective dealloying method to create multiscale porous metals. Currently, there are three types of chemical dealloying fabrication methods for multiscale porous metals: 1) two-step dealloying method ²³, 2) dealloying of intermetallic and metallic elemental phases method ²⁴, which uses various binary alloy systems as the precursors, and 3) ternary alloy dealloying method ²⁵, which uses ternary precursor alloys.

Using the two-step dealloying method, Ding *et al.* ²³ fabricated bimodal porous Au by dealloying of Ag-Au alloy. The first dealloying step forms nanoporous Au (NPG) with pore size of 10-100 nm, which was then electrolessly plated with silver and annealed to simultaneously form Ag-Au alloy and coarsen the initial NPG; after the second dealloying step, a bimodal porous Au was formed with pore sizes of 1-2 μ m and 8 nm. Dealloying of intermetallic and metallic elemental phases method was demonstrated by Song *et al.* ²⁴: They fabricated porous Cu containing micron-sized (tens of micrometers) and nano-sized pores (50-200 nm) by dealloying of annealed Cu-75 at. % Al alloy composed of intermetallic CuAl₂ phase and α -Al (Cu) phases. However, dealloying of binary precursor alloys to fabricate multiscale porous metals remains as a relatively complicated technique and has limitations in the range of porosity it can produce.

Dealloying of ternary precursor alloys is an effective method to fabricate multiscale porous metals. Zhang *et al.* fabricated bimodal nanoporous bimetallic Pt–Au alloy through one-step dealloying of Al-Pt-Au ternary precursor alloys ²⁶. Subsequently, they fabricated bimodal porous Pd-Au with finer AuPd nanoporous structure and coarser Pd(Au) nanoporous structure by dealloying Al–Pd–Au ternary alloy ²⁷. Multiscale porous Cu-Ti bimetallic electrocatalyst fabricated by Qi Lu, et al. ²⁸ shows high hydrogen evolution activity due to the bimodal structure: the micro-scale pores

improve the mass transport and the nanopores provide large-surface area for electrocatalytic hydrogen evolution. Qiu, *et al.* designed a bimodal porous Au to enhance the electrocatalytic activity and support the fabrication of an oxidase-based biosensor ²⁹. Currently, most of the multiscale porous metallic materials prepared by ternary alloy dealloying method are porous alloys instead of pure porous metals. There are limited studies on pure multiscale porous metals fabricated by dealloying ternary alloy due to the difficulty in selecting adequate ternary precursor alloy systems and compositions.

Porous Cu has excellent properties: high electrical and thermal conductivities, ductility, nontoxicity and low cost, which makes porous copper and its derived materials become excellent candidates in a range of applications, such as energy storage and conversion materials, filters, electrochemically or chemically driven actuators and catalysts ³⁰. Multiscale porous Cu exhibits high cycling performance as a current collector ^{31 32}, excellent surface—enhanced Raman scattering (SERS) as a sensor ³³ and high thermal management performance as a heat pipe ³⁴.

Currently, except for dealloying of intermetallic and metallic elemental phases methods demonstrated by Song et al. mentioned above, other methods have also been used to fabricated multiscale bimodal porous Cu. Shin et al. ³⁵ fabricated a variety of bimodal porous Cu using gas deconvolution in an electrochemical deposition process. CuSO₄ and H₂SO₄ are the salts used for porous Cu formation. The bimodal pore size can be adjusted in the range of 20-100 µm and 50-300 nm. Some pore size gradient has been observed in this method. Liu et al. ³⁶ fabricated bimodal porous Cu through vacuum dealloying combining with chemical dealloying method using Zn₇₀Cu₃₀ precursor alloy. The bimodal pore sizes are in the range of 0.5-3.5 µm and 200 nm. Luo et al. ³¹ obtained bimodal porous Cu with irregular micro-porosity (pore size: 0.5-1 µm) and nano-porosity (pore size: 200-300 nm) by chemical dealloying of Cu-34Zn-6Al (wt. %) ternary precursor alloy. However, the bimodal porous Cu prepared by the latter two methods result in a structure with nano-sized pores distributing on the surface of micron-sized ligaments.

In this study, we studied bimodal porous Cu with high porosity, nano-sized pores and micronsized pores fabricated via a simple one step chemical dealloying method using Cu-Fe-Al ternary alloys as the precursor. The selection of Cu-Fe-Al ternary alloy system is based on the different mixing enthalpies principle: when $\Delta H < 0$, the compatibility between elements is good, and when Δ H>0, the elements are immiscible, which has been discussed in detail in our previous work ³⁷. In order to precisely control the structure of the bimodal porous Cu, the effect of phase composition and microstructure of precursor alloys on the bimodal porous structure was systematically studied. The phase composition was determined via synchrotron X-ray diffraction refinement. Moreover, the 3D morphology of precursor Cu-Fe-Al ternary alloy and corresponding bimodal porous Cu were characterized by advanced synchrotron X-ray nano-tomography. The 3D morphological parameters of bimodal porous Cu were quantified to establish the processing-structure correlation for the ternary alloy dealloying method. The specific surface area and transport properties of porous metals are particularly important when they are used as functional materials. Tortuosity (the effective diffusion path length divided by the straight distance) is an important parameter determining the transport properties of porous materials. Therefore, tortuosity of bimodal porous Cu was quantified in this study. This work provides a guide for porous structure design through controlling phase composition in precursor alloys, so that various multiscale porous structure can be precisely constructed, tailored to specific potential applications.

2. Methods

2.1 Fabrication of Precursor Alloys and Bimodal Porous Cu and microstructure analysis

Metal powders of Cu (99 wt% purity, 1 µm average particle size, Alfa Aesar), Fe (99.5 wt% purity, 8 µm, Alfa Aesar) and Al (99.5 wt% purity, 2 µm, Aladdin Industrial Corporation) with spherical geometry were mixed through a two-dimensional low energy ball milling apparatus (QM-

A light ball milling machine, Xianyang, China). The mixed powders were then used to prepare a series of ternary precursor alloys with constant Cu content: 25 at. %, and adjustable Al content: from 10 at. % to 60 at. % and Fe content: from 65 at. % to 15 at. %: Al_xFe₇₅Cu_{25-x}, x=10, 20, 30, 40, 50 and 60. Different Cu, Fe and Al particle sizes were chosen in order to form homogenous and dense precursor alloys during powder metallurgy sintering process. The precursor alloys were sintered at 800 °C for 5 min in vacuum by Plasma Activated Sintering (PAS) facility (ED-PAS 111, Japan) with a sintering pressure of 50 MPa. The precursor alloys (cylindrical shape) with 25 mm diameter and 11 mm thickness after sintering were then machined into cylinders with 5 mm diameter and 10 mm thickness. Subsequently, chemical dealloying method was applied to fabricate multiscale porous Cu. The Cu-Fe-Al precursor alloys were immersed into 5 wt. % sulfuric acid (H₂SO₄) aqueous solution at 90 °C; when the dealloying completed, no gas bubbles from hydrogen gas evolution emerged in the solution. It takes about 20 h to finish the dealloying process for the alloy (cylindrical shape) with 5 mm diameter and 10 mm thickness. Deionized (DI) water was used to prepare the H₂SO₄ solution. The fully dealloyed samples were immersed in DI water and then ethanol consecutively for about 20 min in each step. The chemistry-fabrication scheme of bimodal porous Cu material with nano-sized and micron-sized pores is shown in Figure 1.

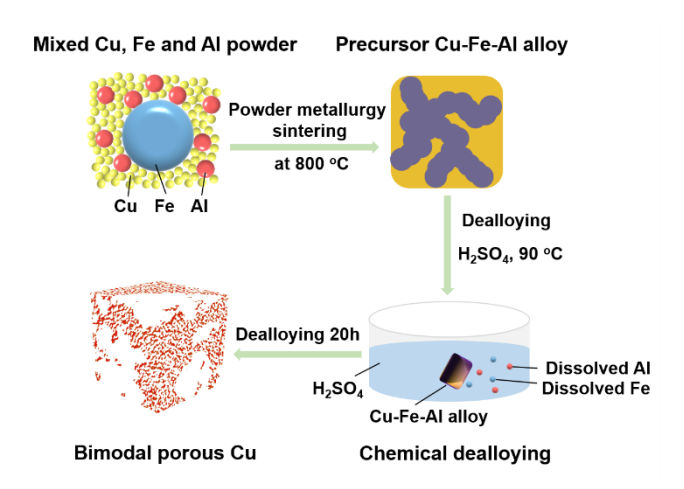


Figure 1 - The chemistry-fabrication scheme of bimodal porous Cu material with nano-sized and micron-sized pores.

The surface microstructure of Cu-Fe-Al precursor alloys and cross-section microstructure of porous Cu were investigated through scanning electron microscopy (SEM) at the Center for Functional Nanomaterials (CFN) at Brookhaven National Laboratory (BNL).

2.2 Synchrotron X-ray Powder Diffraction (XPD) Characterization

The phase composition of six different Cu-Fe-Al precursor alloys were analyzed at 28-ID-2 X-ray Powder Diffraction (XPD) beamline, National Synchrotron Light Source II (NSLS-II), BNL. The detector is PerkinElmer amorphous silicon flat-panel with 2048 (H) x 2048 (V) pixels and 200 µm x 200 µm pixel size. In order to minimize the effect of gasket to the diffraction pattern, the beam (52.38 keV) was collimated to about 0.3 mm x 0.2 mm. Pure nickel powder was used as a standard to determine the geometric parameters including the detector-to-sample distance, and the FIT2D program was used for radial integration of the two-dimensional data ³⁸. Rietveld refinements of the obtained synchrotron diffraction data were performed using the TOPAS V3.0 software ³⁹.

2.3 Sample preparation for X-ray Nano-tomography Characterization

Based on the phase composition and microstructure analysis results, four representative precursor alloys (Al_xFe_{75-x}Cu₂₅, x=10, 30, 50, 60) and their corresponding porous Cu were selected to conduct X-ray nano-tomography characterization. All samples measured in X-ray nano-tomography characterization were prepared by focused ion beam (FIB) milling and lift-out at the CFN of BNL. The precursor alloy samples and porous Cu samples were milled into micro-pillars by 21 nA ion beam current in selected regions, and the surface of micro-pillars were cleaned by 2.8 nA ion beam current. Then the micro-pillars were cut off by 9.3 nA ion beam, lifted out, and attached onto a sharp W pin by Pt deposition following an established procedure published previously ⁴⁰. The final cylinders were in the dimension of 25-30 μm in diameter and ~50 μm in length.

2.4 Synchrotron Transmission X-ray microscopy characterization

Synchrotron X-ray nano-tomography characterization was conducted at the Full-field X-ray Imaging (FXI) Beamline 18-ID, NSLS-II, BNL. FXI beamline has the full field transmission X-ray microscopy (TXM) at FXI beamline with the capability to conduct a full 3D nano-tomography dataset within one-minute acquisition time ⁴¹. The TXM utilizes a capillary condenser, and a 30 nm outermost Fresnel zone plate as an objective lens. The X-ray projection images of the samples were collected on an Andor Neo 5.5 detector with 2560 (H) x 2160 (V) pixels and 6.5 μm x 6.5 μm pixel size. A flyscan mode was used with a rotation range from 0 to 180°, rotation speed of 2 deg/s and an exposure time of 0.045 s. Finally, 1080 projections images (2 x 2 binned) were recorded with a pixel size of 34 nm. The incident X-ray energy used to conduct this work was at 9.1 keV (above Cu K-edge), 8.95 keV (below Cu K-edge), 7.2 keV (above Fe K-edge) and 7.1 (below Fe K-edge) keV, respectively.

2.5 Data Processing and Analyzation

The X-ray nano-tomography data was reconstructed using the "Gridrec" implementation in Tomopy via a filtered-back projection (FBP) algorithm ⁴². The different phases in precursor alloys and pores and ligament in porous Cu in the reconstructed images were segmented using Trainable Weka Segmentation, a machine learning algorithm, in freeware Image J ⁴³ ⁴⁴. 3D median filter with a kernel size of 2×2×2 was performed in the segmented images. A commercial software, Avizo (v.9.3 FEI), was used to visualize of 3D morphology. A customized Matlab code developed in-house by implementing well-established methods was applied to the segmented 3D images to quantify tortuosity ⁴⁵ and the size distribution ⁴⁶ of pores, ligaments and phases in precursor alloys in three dimensions. The "quasi-Euclidean" voxel neighboring definitions algorithm ⁴⁵ was applied to calculate tortuosity. The volume fraction of pores and ligaments was determined according voxel counting in the image histogram in freeware Image J. Furthermore, Mercury Porosimetry (AutoPore IV-9500 V1.05) were also used to characterize the pore size distribution of bulk bimodal porous Cu to complement the analysis from X-ray nano-tomography, where the sample dimension was limited

by the X-ray attenuation and the field of view of the microscope.

3. Results and Discussion

3.1 Effect of Phase Composition of Precursor Alloys on morphology of multiscale porous Cu

The phase composition and morphology of precursor alloys directly affect the microstructure of corresponding porous metals fabricated by dealloying method. In this study, Cu, Fe and Al metal powders with a range of different ratios were used to fabricate precursor Cu-Fe-Al alloys (Al_xFe₇₅-_xCu₂₅, x=10, 20, 30, 40, 50 and 60) with different phase compositions, which creates various porous structures after dealloying. Synchrotron x-ray powder diffraction (XPD) was conducted to identify the phase composition and crystal structure of Cu-Fe-Al precursor alloys via refinement, as shown in Figure 2 (a-1)-(f-1). Fm-3m face-centered cubic (FCC) crystal structure Cu-rich phases and Im-3m body-centered cubic (BCC) crystal structure Fe-rich phases are observed in both of Al₁₀Fe₆₅Cu₂₅ and Al₂₀Fe₅₅Cu₂₅ precursor alloys. Therefore, from the back-scattering mode of SEM images in Figure 2 (a-2) and (b-2), it can be clearly distinguished that the bright area is Cu-rich phase with relatively higher atomic number (Z), and the dark area is Fe-rich phase with relatively lower Z. With the Al content increasing to 30 at. %, the Pm-3m CsCl type (B2) crystal structure Cu_{0.45}Fe_{0.7}Al_{0.85} phase appears, and there is also a very small amount of unknown phase which cannot be identified because of the low intensity in its X-ray signal, so that there are four phases in Al₃₀Fe₄₅Cu₂₅ precursor alloy, as shown in Figure 2 (c-1); note that here the intensity of Cu-rich phase becomes quite low. With continuing increasing of Al content to 40-50 at. %, there is only B2 crystal structure Cu_{0.48}Fe_{0.72}Al_{0.8} phase in Al₄₀Fe₃₅Cu₂₅ alloy and B2 crystal structure Cu_{0.50}Fe_{0.56}Al_{0.94} phase in Al₅₀Fe₂₅Cu₂₅ precursor alloy. Because the less amount of densification of Cu_{0.48}Fe_{0.72}Al_{0.8} and Cu_{0.5}Fe_{0.56}Al_{0.94} phases, some continuous cracks and voids can be observed in Al₄₀Fe₃₅Cu₂₅ and Al₅₀Fe₂₅Cu₂₅ precursor alloys, seen as the dark area in Figure 2 (d-2) and (e-2). In the precursor with 60 at. % of Al, B2 crystal structure

Cu_{0.9}Fe_{0.2}Al_{0.9} phase (the phase with relative higher *Z*) and C/2m monoclinic crystal structure CuFe₄Al₁₂ intermetallic phase (the phase with relatively lower *Z*) are formed in Al₆₀Fe₁₅Cu₂₅ precursor alloys. The synchrotron X-ray powder diffraction (XPD) refinement results of six different precursor alloys are shown in supporting information Figure S1 and Table S1.

After chemical dealloying using 5 wt% sulfuric acid (H₂SO₄) aqueous solution at 90 °C, all the six precursor alloys are fully dealloyed (as shown in Figure S 2) and form multiscale porous structure, regardless of the composition and number of phases are contained in precursor alloy. However, the pore size of microporous structure formed by dealloying of Al₄₀Fe₃₅Cu₂₅ and Al₅₀Fe₂₅Cu₂₅ precursor alloys is smaller than the other compositions, as shown in Figure 2 (a-3)-(f-3). For the precursor alloy with low content of Al, only little amount of nanoporous structure formed on the surface of micronsized pore's ligaments. When the Al content increases to 30 at. % or even higher than 30 at. %, the whole ligaments of micron-sized pores become nanoporous structure.

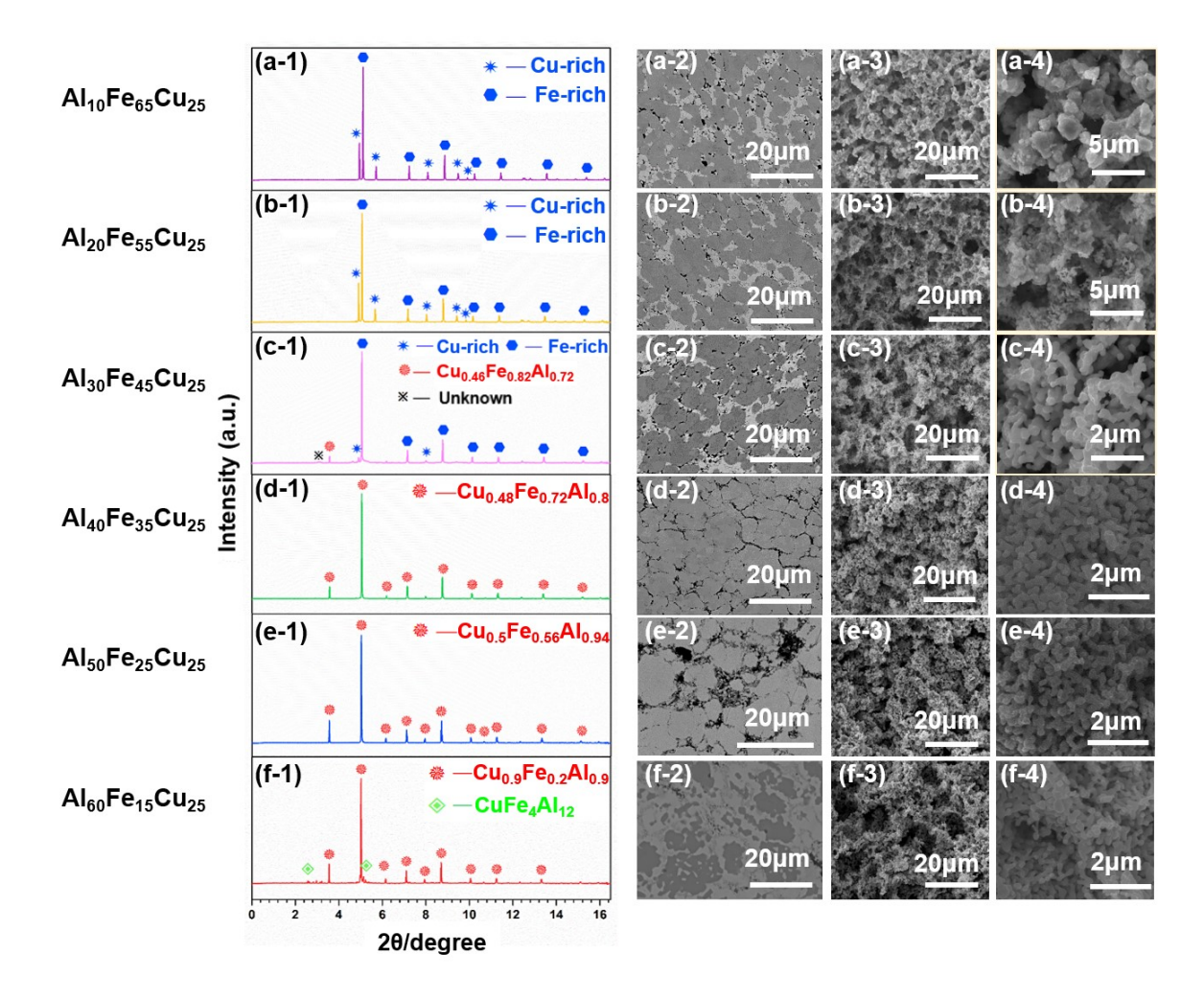


Figure 2 - Phase composition and microstructure of precursor alloys and their corresponding porous Cu after dealloying in 5wt. % H₂SO₄ aqueous solution at 90 °C. The compositions of precursor alloys: (a) Al₁₀Fe₆₅Cu₂₅, (b) Al₂₀Fe₅₅Cu₂₅, (c) Al₃₀Fe₄₅Cu₂₅, (d) Al₄₀Fe₃₅Cu₂₅, (e) Al₅₀Fe₂₅Cu₂₅, (f) Al₆₀Fe₁₅Cu₂₅. Synchrotron X-ray powder diffraction (XPD) patterns showing phase composition of precursor alloys (a-1) - (f-1); back-scattering mode of scanning electron microscope (SEM) images showing the microstructure of precursor alloys (a-2) - (f-2) and corresponding porous Cu (a-3) - (f-3) and zoom-in view of porous structure (a-4) - (f-4).

Synchrotron X-ray nano-tomography characterizes the 3D morphology of four representative

Cu-Fe-Al precursor alloys (Al_xFe_{75-x}Cu₂₅, x=10, 30, 50, 60) and their corresponding fully dealloyed multiscale porous Cu, as shown in Figure 3. In Figure 3 (a), Cu-rich phase (light blue color) formed in Al₁₀Fe₆₅Cu₂₅ alloy-exhibits a 3D continuous structure. The volume of Fe-rich phase (yellow color) in this alloy is larger than the Cu-rich phase. For Al₃₀Fe₄₅Cu₂₅ alloy, the unknown phase will not be considered in the following discussion due to the low content. Because the volume percent of Cu-rich phase in Al₃₀Fe₄₅Cu₂₅ alloy is quite low (as shown in Table S1) and beyond the limitation of accurate segmentation. We labeled the Cu-rich and Cu_{0.45}Fe_{0.7}Al_{0.85} phases as a mixed phase, marked with pink color (Figure 3 (b)). When the Al content increases to 50 at. %, only Cu_{0.5}Fe_{0.56}Al_{0.94} phase (light green color) and cracks and voids (black color) can be observed in the precursor alloy. Moreover, we can observe cracks and voids in the structure likely caused by incomplete densification during the sintering process. In Al₆₀Fe₁₅Cu₂₅ alloy, in addition to Cu_{0.9}Fe_{0.2}Al_{0.9} phase (red blue color), there is also CuFe₄Al₁₂ phase (dark blue color), whose shape and size are not homogeneous.

The difference of 3D morphology between Cu-Fe-Al precursor alloys leads to the variety of multiscale porous structure after dealloying. Through comparing the chemical activity and 3D morphology of different phases in precursor alloys and 3D morphology of porous structure, it can be identified that the micron-sized pores in multiscale porous Cu are formed due to the dissolution of Fe-rich phase in both Al₁₀Fe₆₅Cu₂₅ alloy and Al₃₀Fe₄₅Cu₂₅ alloy, and CuFe₄Al₁₂ phase in Al₆₀Fe₁₅Cu₂₅ alloy. With the dissolution of Al and Fe active components, the active (less noble) components (Fe and Al) rich phase forms a nanoporous structure firstly; then, the undissolved Fe and Al components in the nano-ligaments were gradually dissolved until the dissolution was complete. Because these active components rich phases contain no or little amount of Cu, the Cu content is not sufficient to form a continuous network structure after the dissolution of Fe and Al, and thus a microporous

structure forms. The specific formation mechanism of micron-sized pores has been discussed in our prior work ³⁷. The nanoporous structure was formed by dealloying of other phases in the four representative precursor alloys: Cu-rich, Cu_{0.45}Fe_{0.7}Al_{0.85}, Cu_{0.5}Fe_{0.56}Al_{0.94} and Cu_{0.9}Fe_{0.2}Al_{0.9} phases. Note that while micron-sized pores can also be observed in porous Cu after dealloying of Al₅₀Fe₂₅Cu₂₅ alloy, which has just one phase, due to the contribution of the initial voids in precursor alloy; the morphology of microporous structure in Figure 3 (g) is similar with the voids in Figure 3 (c). The porous Cu fabricated by dealloying of Al₁₀Fe₆₅Cu₂₅ alloy exhibits the most homogenous microporous structure, but there is only little amount of nanoporous structure formed due to the low content of Al. With the Al content increasing to 30 at. % or higher in precursor alloys, all of the micron-sized ligaments in their corresponding porous Cu are composed of nanoporous structure, which can be seen in Figure 3 (f)-(h) and the zoom-in view Figure 3 (j)-(l). The multiscale porous Cu formed by dealloying Al₅₀Fe₂₅Cu₂₅ alloy possesses the largest volume of nanoporous structure; this is because there is only Cu_{0.5}Fe_{0.56}Al_{0.94} phases which forms nanopores in Al₅₀Fe₂₅Cu₂₅ alloy, and the volume of initial cracks and voids caused by incomplete sintering densification is relatively low. Moreover, comparing Figure 3 (k) and (l) with Figure 3 (j) from tomography analysis, the nano-ligament size of porous Cu dealloyed from Al₅₀Fe₂₅Cu₂₅ and Al₆₀Fe₁₅Cu₂₅ alloys is smaller than that dealloyed from Al₃₀Fe₄₅Cu₂₅ alloy.

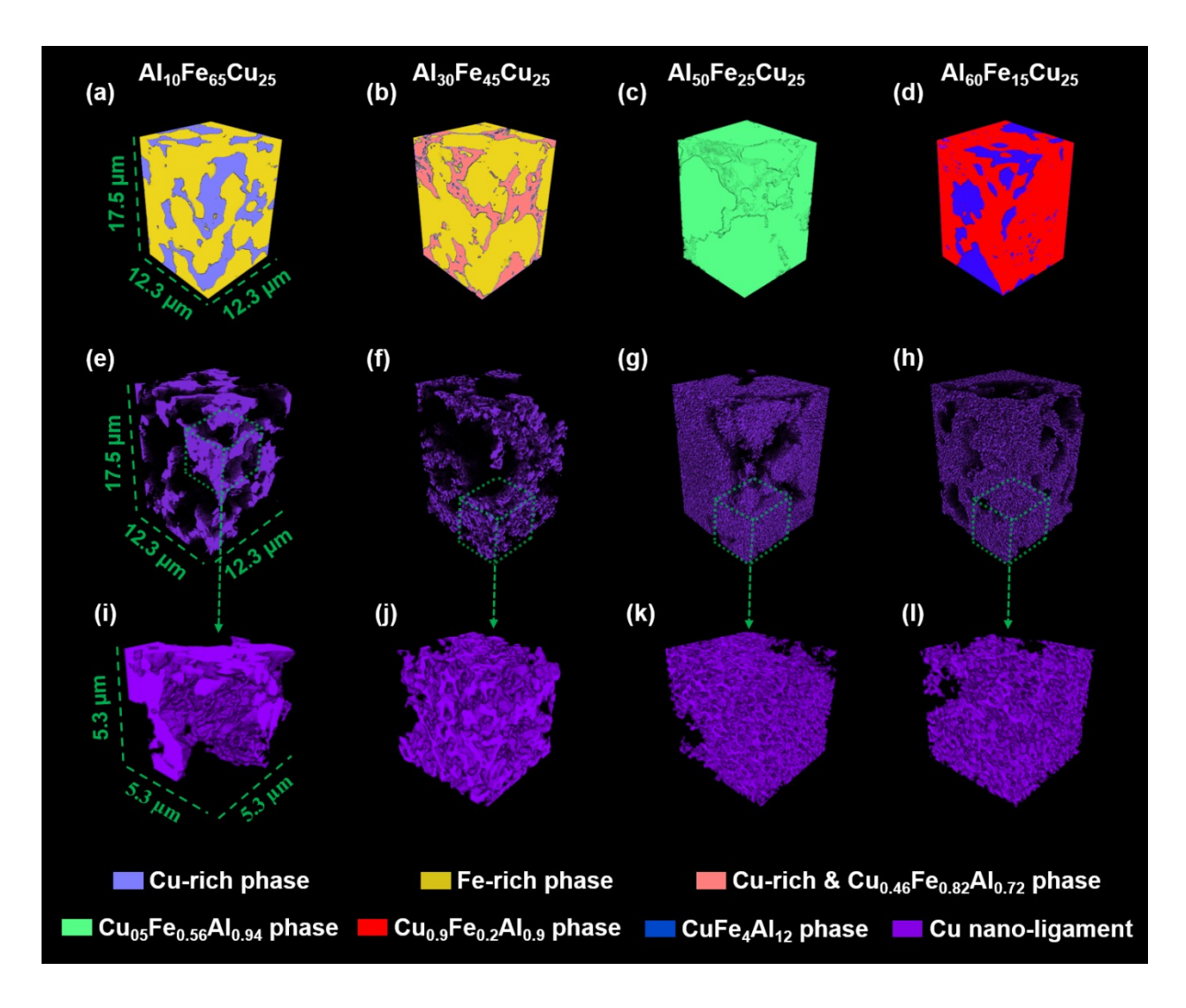


Figure 3 - 3D morphology of Cu-Fe-Al precursor alloys and their corresponding fully dealloyed, multiscale porous Cu. X-ray nano-tomography reconstruction showing the 3D morphology: (a) – (d) Al₁₀Fe₆₅Cu₂₅, Al₃₀Fe₄₅Cu₂₅, Al₅₀Fe₂₅Cu₂₅ and Al₆₀Fe₁₅Cu₂₅ precursor alloys, (e) – (h) corresponding multiscale porous Cu with micron- and nano-sized pores; a zoom-in view of shown in (i) – (l): a 'zoom-in' view of 3D morphology of the nanoporous structure cropped from a volume marked by green dash rectangle in (e)-(h).

3.2 Quantification of morphological parameters of multiscale porous structure

In order to further explore the relationship between precursor alloys and multiscale porous structure,

the 3D morphology of four representative precursor alloys: Al₁₀Fe₆₅Cu₂₅, Al₃₀Fe₄₅Cu₂₅, Al₅₀Fe₂₅Cu₂₅ and Al₆₀Fe₁₅Cu₂₅ and their corresponding multiscale porous Cu are compared here through quantitative calculation of different morphology parameters, as shown in Figure 4. From Figure 4 (a): it can be found that with the increase of Al content in precursor alloys, the ligament size of their corresponding porous Cu decreases gradually. The ligament size of porous Cu after dealloying of $Al_{60}Fe_{15}Cu_{25}$ alloy is just ~100 nm. In contrast, the ligament size of porous Cu after dealloying of Al₁₀Fe₆₅Cu₂₅ alloy shows a wider distribution: from nanometer to micrometer. The pore size distribution of porous Cu in Figure 4 (b) shows that the pore size of dealloyed Al₁₀Fe₆₅Cu₂₅ is primarily in micrometer size range, with only little amount of nano-sized pores. The other three types of porous Cu show distinct multiscale bimodal porous structure. The nano-sized pores of the multiscale porous Cu after dealloying of Al₅₀Fe₂₅Cu₂₅ and Al₆₀Fe₁₅Cu₂₅ alloys is quite similar and smallest. With Al content of precursor alloy decreasing to 30 at. %, nano-sized pores become larger. According to the prior discussions, we know that the nanoporous structure from dealloying of Al₅₀Fe₂₅Cu₂₅ and Al₆₀Fe₁₅Cu₂₅ alloys is formed by dealloying B2 crystal structure phase, and nanoporous structure from dealloying of Al₁₀Fe₆₅Cu₂₅ and Al₃₀Fe₄₅Cu₂₅ alloys is formed by dealloying FCC crystal structure phase. Therefore, it indicates that the pore size through dealloying B2 crystal structure phase is smaller than dealloying FCC crystal structure phase. Meanwhile, the size distribution of micron-sized pores in different porous Cu does not follow a specific trend, and it mainly depends on the size of the corresponding dissolving phases in precursor alloys, because they have the same size distribution trend. This can be further understood through results in Figure 4 (c) and (d).

Figure 4 (c) shows the size distribution of the phases in precursor alloys that form nanoporous

structure after dealloying: the Cu-rich phase (light blue color in Figure 3a) in $Al_{10}Fe_{65}Cu_{25}$ alloy, the Cu-rich and $Cu_{0.46}Fe_{0.82}Al_{0.72}$ mixed phase (pink color in Figure 3b) in $Al_{30}Fe_{45}Cu_{25}$ alloy, the $Cu_{0.5}Fe_{0.56}Al_{0.94}$ phase (light green color in Figure 3c) in $Al_{50}Fe_{25}Cu_{25}$ alloy and the $Cu_{0.9}Fe_{0.2}Al_{0.9}$ (red color in Figure 3d) phase in $Al_{60}Fe_{15}Cu_{25}$ alloy, which is denoted as higher-*Z*-phase (it is named on the basis of the relative atomic number *Z* and contrast in SEM images in Figure 2). The size distribution of the phases that form microporous structure is shown in

Figure 4 (d): Fe-rich phase (yellow color in Figure 3a-b) in Al₁₀Fe₆₅Cu₂₅ and Al₃₀Fe₄₅Cu₂₅ alloys, the cracks and voids (black uneven area in Figure 3c) in Al₅₀Fe₂₅Cu₂₅ alloy and CuFe₄Al₁₂ phase (dark blue color in Figure 3d) in Al₆₀Fe₁₅Cu₂₅ alloy, which is denoted as lower-Z-phase. The average size of the higher-Z-phase in Al₁₀Fe₆₅Cu₂₅ and Al₃₀Fe₄₅Cu₂₅ alloys is about 1µm and smaller than the other two precursor alloys. The higher-Z-phase in Al₅₀Fe₂₅Cu₂₅ alloy is the largest, which is consistent with the morphology in Figure 3. In contrast, lower-Z-phase in Al₅₀Fe₂₅Cu₂₅ alloy shows the smallest size, including voids from nanometer to micrometer, because it is formed from incompletely sintering densification. The size of the lower-Z-phase that forms micron-sized pores after dealloying of Al₅₀Fe₂₅Cu₂₅, Al₆₀Fe₁₅Cu₂₅, Al₃₀Fe₄₅Cu₂₅ and Al₁₀Fe₆₅Cu₂₅ alloys increase gradually, which has the same trend as the micron-sized pore shown in Figure 4 (b). Because of the sample volume size limitation here in X-ray nano-tomography, it cannot evaluate the distribution of micron-sized pores accurately. Therefore, the pore size distribution of bulk porous Cu was characterized using Mercury Porosimetry, as shown in Figure 4 (e). The volume fraction of pores should be similar in this series of Cu-Fe-Al precursor alloys due to the same content of Cu. However, in Figure 4 (f), the volume fraction of pores after dealloying of Al₅₀Fe₂₅Cu₂₅ alloy is lower than the other samples. This may be due to the region-to-region variation when selecting sample volume for quantitative calculation,

because the size of initial cracks and voids in Al₅₀Fe₂₅Cu₂₅ alloy is quite inhomogeneous, as shown in Figure 4 (d).

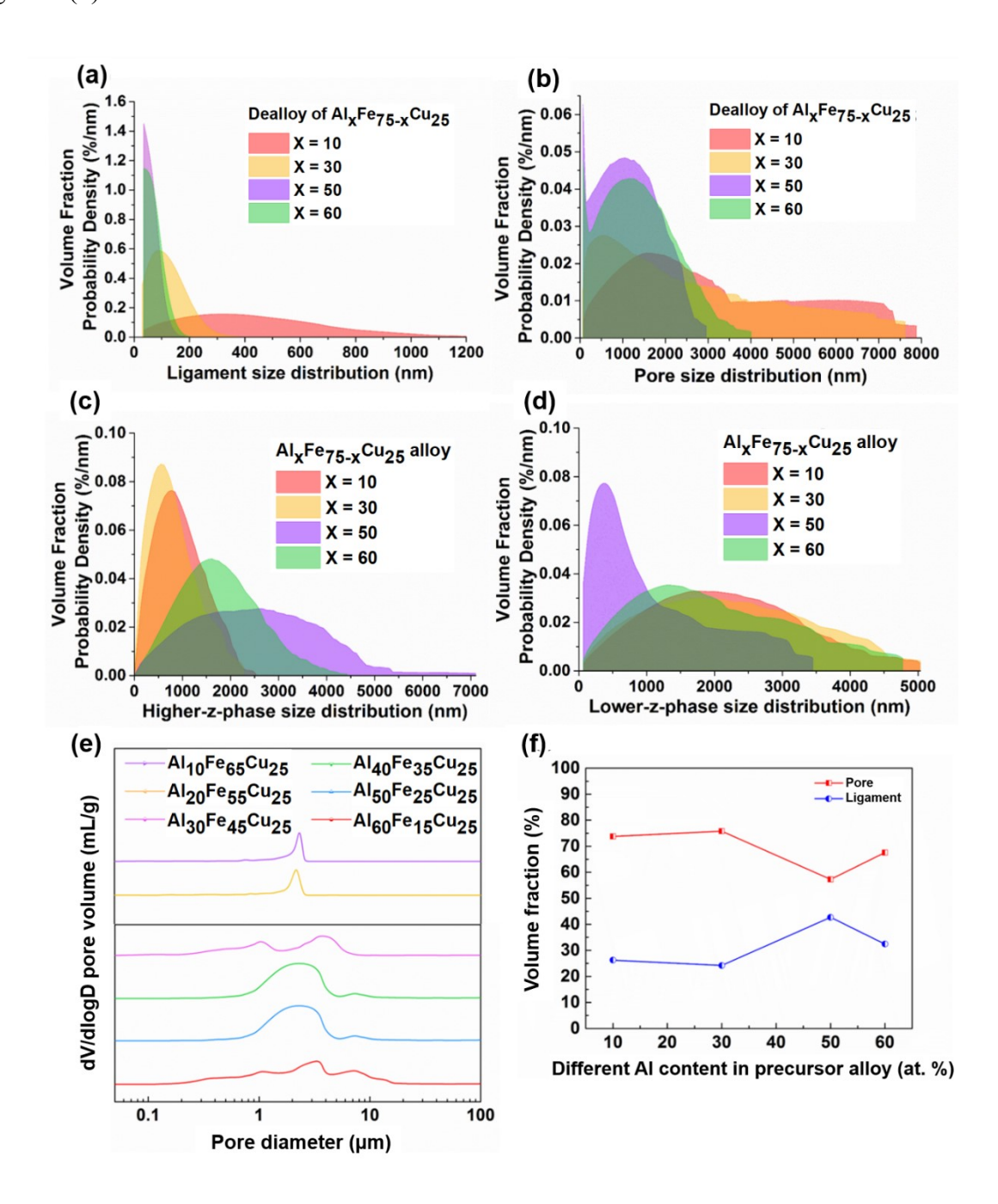


Figure 4 - (a) Ligament size distribution and (b) pore size distribution, quantified according to the segmented 3D images of fully dealloyed of $Al_xFe_{75-x}Cu_{25}$, x=10, 30, 50 and 60 precursor alloys at 90 °C. (c) higher-Z-phase (which represents the phase with relatively higher atomic number Z and relatively higher contrast as shown in SEM images in Figure 2) size distribution and (d) lower-Z-

phase (which represents the phase with relatively lower Z and relative lower contrast as shown in SEM images in Figure 2) size distribution of Al₁₀Fe₆₅Cu₂₅, Al₃₀Fe₄₅Cu₂₅, Al₅₀Fe₂₅Cu₂₅ and Al₆₀Fe₁₅Cu₂₅ precursor alloys. (e) Pore size distribution of fully dealloyed precursor alloys bulk sample characterized using Mercury Porosimetry. (f) Volume fraction of 3D morphological parameters: pores and ligaments.

The effective diffusivity and conductivity for porous media can be quantitatively reflected through an important geometric parameter — tortuosity which is the ratio between a tortuous path distance and a straight distance ^{47 45}. 3D distance maps are shown in Figure 5 to directly quantify and visualize the tortuosity based on geometric propagation. Although all three orthogonal directions, each with both positive and negative propagating directions, were calculated, only the 3D path distance maps along positive direction of x axis is displayed here as a representation, because the multiscale porous Cu is a three-dimensionally homogenous structure⁴⁸. In Figure 5 (a)-(d), the color bar shows the actual propagating path distance. The white lines marked in 3D path distance maps are three different x locations along y direction, which represents the straight distance of 3.52 μm, 7.04 μm and 10.56 μm, respectively.

Combining 3D path distance maps in Figure 5 (a)-(d) and distance profiles in Figure 5 (i)-(l), it can be found that the more homogeneous of the ligament size distribution, the more homogeneous of the actual path distance along y direction in the three selected specific x locations in porous Cu. Therefore, the porous Cu from dealloying Al₁₀Fe₆₅Cu₂₅ alloy shows the most inhomogeneous propagation front., which is due to the existence of small amount of nanoporous structure on the surface of some micro-ligaments. However, the ligaments of Cu porous structure from dealloying Al₃₀Fe₄₅Cu₂₅ and Al₆₀Fe₁₅Cu₂₅ precursor alloys are quite homogeneous and all in nano size, so that

the actual propagation front in these alloys is more uniform, compared with the micro-porous structure from dealloying Al₁₀Fe₆₅Cu₂₅ alloy. From the spatial distribution maps of tortuosity in x direction in Figure 5 (e)-(h), the tortuosity of all these four porous Cu is relatively low, with the highest tortuosity ~1.07, which is beneficial for ionic transport through the porous structure. Bae et al. has demonstrated this via artificially engineered battery electrodes ⁴⁹. The porous Cu after dealloying of Al₅₀Fe₂₅Cu₂₅ alloy exhibits the highest tortuosity because it owns the lowest volume fraction of micron-sized pore; the tortuosity of the other three porous structure is lower, which shows that the micron-sized pores can compensate the increase of the diffusion path length due to nanoporosity, facilitating diffusion within a porous structure.

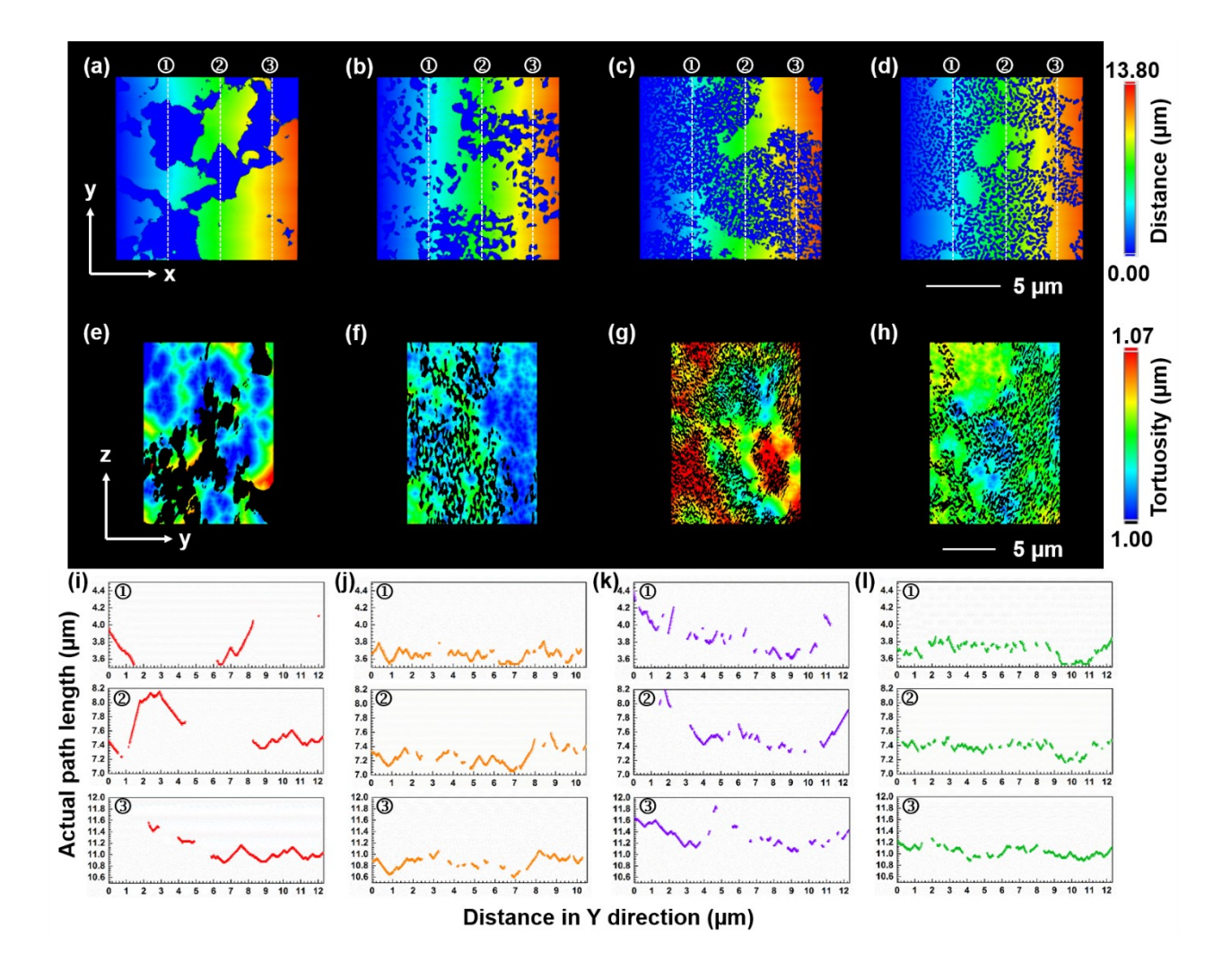


Figure 5 – Tortuosity, 3D distance map and distance profiles at three specific position based on geometric propagation within the pore phase of multiscale porous Cu after dealloying of Al_xFe_{75-x}Cu₂₅, x=10, 30, 50 and 60 precursor alloys. (a)-(d) 3D distance map propagating along the positive x direction, (e)-(h) spatial distribution maps of tortuosity in x direction, (i)-(l) distance profiles showing the actual diffusion path length of multiscale porous Cu at three different x locations as indicated in (a)-(d).

Finally, the relationship between individual typical phases and their corresponding porous morphology after dealloying is summarized in Figure 6. The FCC and B2 structure phases with higher noble metallic atom content (Cu in this study) will form nanoporous structure after dealloying; among them, the B2 structure phase has relative lower noble atom content, so that the nanopores and nanoligaments size will be smaller. However, when the content of the noble metallic atom in a precursor phase is too low to form a continuous network structure after dealloying, the whole phase will be fully dissolved and form porous structure with the same size as the corresponding precursor phase, for example BCC and monoclinic structure phase. Therefore, if the FCC, BCC, B2 and monoclinic crystal structure phases and their corresponding morphology after dealloying are considered as the 'building blocks', various multiscale porous Cu with specific morphology can be designed through mixing different individual 'building' blocks. Therefore, Al₁₀Fe₆₅Cu₂₅, Al₂₀Fe₅₅Cu₂₅, Al₃₀Fe₄₅Cu₂₅ and Al₆₀Fe₁₅Cu₂₅ alloys will form bimodal porous structure after dealloying, and their pore size and ligament size will decrease gradually. Because Al₄₀Fe₃₅Cu₂₅ and Al₅₀Fe₂₅Cu₂₅ alloys only have one Cu₄Fe₆Al₁₂ phase, they will theoretically form single-modal nanoporous structure. However, by introducing voids from incomplete densification during sintering, Al₄₀Fe₃₅Cu₂₅ and Al₅₀Fe₂₅Cu₂₅ alloys can also formed bimodal porous structure after dealloying.

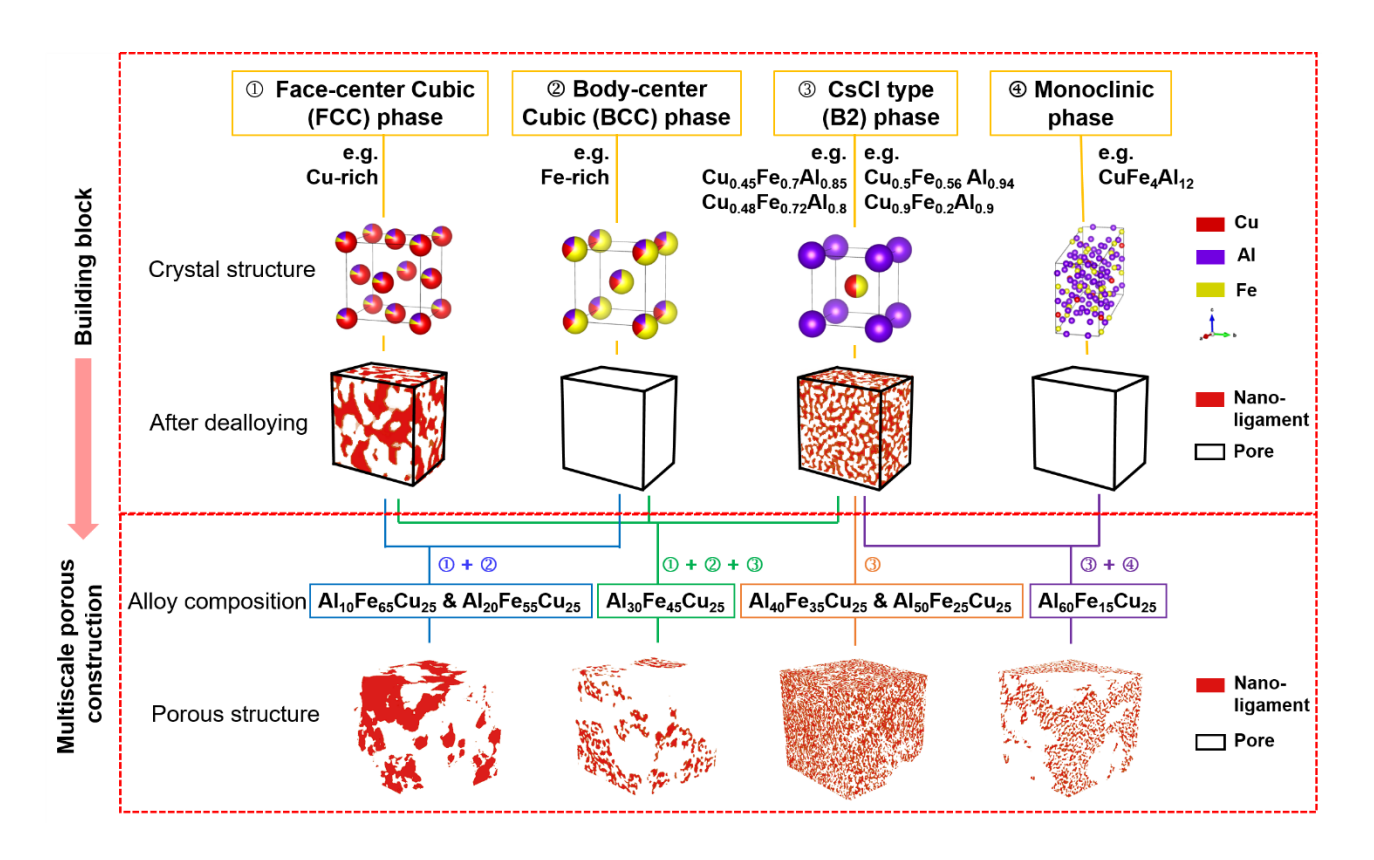


Figure 6 - The design concept of various multiscale porous Cu constructions with specific morphology through selecting different 'building blocks'. The Fm-3m, Im-3m, Pm-3m and C2/m crystal structure phases and their corresponding morphology after dealloying are considered as the 'building blocks'.

4. Conclusions

In this study, different types of multiscale porous Cu with both micron-sized pores and nanosized pores were successfully fabricated through chemical dealloying of a series of Cu-Fe-Al precursor alloys: Al_xFe_{75-x}Cu₂₅, x= 10, 20, 30, 40, 50 and 60. According to the phase composition and 3D morphology of four representative precursor alloys and corresponding porous Cu, it can be identified that FCC and B2 crystal structure phases will form nanoporous structure after dealloying, meanwhile BCC and monoclinic crystal structure phases will be dissolved to form microporosity. By combining the analysis of 3D morphology and quantifying 3D morphological parameters, we showed

that the size of nano-sized pore is determined by the component of phase in precursor alloys: the pore size formed by dealloying of B2 crystal structure phase is smaller than that dealloying of FCC crystal structure phase; while the size of micron-sized pore only depends on the initial size of BCC and monoclinic crystal structure phases in precursor alloys. In the case of incomplete sintering, the initial cracks and voids in precursor alloys will also have an impact on the size of microporosity. The multiscale porous Cu exhibits a uniform diffusion propagation front, with relatively low tortuosity of up to ~1.07. The low tortuosity of bimodal porous Cu is beneficial to enhance the transport properties for functional applications. This work provides a guideline to precisely control the multiscale Cu porous structure formed by dealloying of multi-phase ternary Cu-Fe-Al alloys via adjusting the phase compositions. Various porous structure can be designed according to specific applications for optimal performance. Exploring and further testing the design principle to other ternary alloy systems including Cu ternary alloys in the future would be beneficial.

Acknowledgements

The authors thank Gwen Wright (Center for Functional Nanomaterials, CFN) for assisting SEM, Fernando Camino (CFN) for EDS support and sample preparation with FIB-SEM, and Kim Kisslinger for assisting characterization and sample preparation at CFN. The authors thank Michale Maklary (NSLS-II) for sample machining. This research used resources and Full-Field X-ray Imaging Beamline (FXI, 18-ID) of the National Synchrotron Light Source II, a U.S. Department of Energy (DOE) Office of Science User Facility operated for the DOE Office of Science by Brookhaven National Laboratory under Contract No. DE-SC0012704. This research used resources of the Center for Functional Nanomaterials, which is a U.S. DOE Office of Science Facility, at Brookhaven National Laboratory under Contract No. DE-SC0012704. This work is also financially supported by

the National Key Research and Development Program of China (No. 2018YFB0905600, 2017YFB0310400), the National Natural Science Foundation of China (No. 51472188, and 51521001), Fundamental Research Funds for the Central Universities in China, State Key Laboratory of Advanced Electromagnetic Engineering and Technology (Huazhong University of Science and Technology), and the "111" project (No. B13035). This material is based upon work supported by the National Science Foundation under Grant No. DMR-1752839. Karen Chen-Wiegart acknowledges the support provided via the Faculty Early Career Development Program (CAREER) program and Metals and Metallic Nanostructures program of National Science Foundation. Chonghang Zhao and Karen Chen-Wiegart are grateful for the support of a student fellowship by the Joint Photon Science Institute at Stony Brook University, jointly proposed by Karen Chen-Wiegart as PI and Yong Chu as co-PI and Juergen Thieme and Wah-Keat Lee as collaborators. Chen-Wiegart group members are acknowledged for conducting the FXI and XPD beamtime experiment together and assisting with preliminary analysis: Xiaoyang Liu, Cheng-Hung Lin and Qingkun Meng. Lijie Zou is grateful for the support of the State Scholarship Fund by the China Scholarship Council (CSC).

Author contribution

L. Z., Y.-c. K. C.-W, F. C. and Q.S. developed the research idea. L. Z. and Y.-c. K. C.-W. wrote user proposals for the use of FXI and XPD beamlines at NSLS-II and equipment at CFN; H. W. prepared precursor alloy under the supervision of F. C.; L. Z. conducted dealloying and SEM analysis; L.Z. and C.Z. prepared samples for FXI beamtime. M.G., X.X., and W.L. commissioned and setup the FXI beamline. L.Z., C. Z., M.G., X.X., W.L. and Y.-c. K. C.-W conducted FXI experiment and preliminary data analysis during the experiment together. J. B., H. Z. and S. G. setup the XPD beamline and assisted with data collection. L.Z. conducted FXI data analysis with inputs and guidance from M.G., C.Z. and Y.-c. K. C.-W. and XPD data analysis with guidance from J. B.; F.C. and Y.-c. K. C.-W.

provided scientific insights on data interpretation and mechanistic understanding. L. Z. and Y.-c. K. C.-W. prepared the manuscript, with inputs from other co-authors.

Supporting Information

Further information on experimental methods; further information on refinement analysis results; composition of bimodal porous Cu after dealloying of Cu-Fe-Al alloys; average size from the pore size distribution by Gaussian fitting.

References

- 1. Yun, Q.; He, Y. B.; Lv, W.; Zhao, Y.; Li, B.; Kang, F.; Yang, Q. H., Chemical Dealloying Derived 3D Porous Current Collector for Li Metal Anodes. *Adv Mater* **2016**, *28* (32), 6932-9.
- 2. Zhao, H.; Lei, D.; He, Y.-B.; Yuan, Y.; Yun, Q.; Ni, B.; Lv, W.; Li, B.; Yang, Q.-H.; Kang, F.; Lu, J., Compact 3D Copper with Uniform Porous Structure Derived by Electrochemical Dealloying as Dendrite-Free Lithium Metal Anode Current Collector. *Advanced Energy Materials* **2018**, *8* (19), 1800266.
- 3. Ding, Y.; Chen, M., Nanoporous Metals for Catalytic and Optical Applications. *MRS Bulletin* **2011,** *34* (8), 569-576.
- 4. Wada, T.; Geslin, P.-A.; Kato, H., Preparation of hierarchical porous metals by two-step liquid metal dealloying. *Scripta Materialia* **2018**, *142*, 101-105.
- 5. Liu, Z.; Du, J.; Qiu, C.; Huang, L.; Ma, H.; Shen, D.; Ding, Y., Electrochemical sensor for detection of p-nitrophenol based on nanoporous gold. *Electrochemistry Communications* **2009**, *11* (7), 1365-1368.

- 6. Tuchinskiy, L., Novel Manufacturing Process for Metal and Ceramic Microhoneycombs. *Advanced Engineering Materials* **2008**, *10* (3), 219-222.
- 7. Zhang, J.; Li, C. M., Nanoporous metals: fabrication strategies and advanced electrochemical applications in catalysis, sensing and energy systems. *Chem Soc Rev* **2012**, *41* (21), 7016-31.
- 8. Sang Hoon Joo, S. J. C., Ilwhan Oh, Juhyoun Kwak, Zheng Liu, Osamu Terasaki, Ryong Ryoo, Ordered nanoporous arrays of carbon supporting high dispersions of platinum nanoparticles. *Nature* **2001**, *412*, 169-172.
- 9. An, Y.; Fei, H.; Zeng, G.; Xu, X.; Ci, L.; Xi, B.; Xiong, S.; Feng, J.; Qian, Y., Vacuum distillation derived 3D porous current collector for stable lithium-metal batteries. *Nano Energy* **2018**, *47*, 503-511.
- 10. Shin, H. C.; Liu, M., Three-Dimensional Porous Copper-Tin Alloy Electrodes for Rechargeable Lithium Batteries. *Advanced Functional Materials* **2005**, *15* (4), 582-586.
- 11. Banhart, J., Light-Metal Foams-History of Innovation and Technological Challenges. *Advanced Engineering Materials* **2013**, *15* (3), 82-111.
- 12. Song, T.; Yan, M.; Qian, M., The enabling role of dealloying in the creation of specific hierarchical porous metal structures—A review. *Corrosion Science* **2018**, *134*, 78-98.
- 13. Atwater, M. A.; Guevara, L. N.; Darling, K. A.; Tschopp, M. A., Solid State Porous Metal Production: A Review of the Capabilities, Characteristics, and Challenges. *Advanced Engineering Materials* **2018**, *20* (7), 1700766.
- 14. Juarez, T.; Biener, J.; Weissmüller, J.; Hodge, A. M., Nanoporous Metals with Structural Hierarchy: A Review. *Advanced Engineering Materials* **2017**, *19* (12), 1700389.
- 15. Liu, W. B.; Zhang, S. C.; Li, N.; Zheng, J. W.; Xing, Y. L., A facile one-pot route to fabricate

nanoporous copper with controlled hierarchical pore size distributions through chemical dealloying of Al–Cu alloy in an alkaline solution. *Microporous and Mesoporous Materials* **2011**, *138* (1-3), 1-7. 16. Zhang, Q.; Wang, X.; Qi, Z.; Wang, Y.; Zhang, Z., A benign route to fabricate nanoporous gold through electrochemical dealloying of Al–Au alloys in a neutral solution. *Electrochimica Acta* **2009**, *54* (26), 6190-6198.

- 17. Huang, J. F.; Sun, I. W., Fabrication and Surface Functionalization of Nanoporous Gold by Electrochemical Alloying/Dealloying of Au-Zn in an Ionic Liquid, and the Self-Assembly of L-Cysteine Monolayers. *Advanced Functional Materials* **2005**, *15* (6), 989-994.
- 18. Zhao, C.; Kisslinger, K.; Huang, X.; Lu, M.; Camino, F.; Lin, C.-H.; Yan, H.; Nazaretski, E.; Chu, Y.; Ravel, B.; Liu, M.; Chen-Wiegart, Y.-c. K., Bi-continuous pattern formation in thin films via solid-state interfacial dealloying studied by multimodal characterization. *Materials Horizons* **2019**, 6, 1991-2002.
- 19. Wada, T.; Kato, H., Three-dimensional open-cell macroporous iron, chromium and ferritic stainless steel. *Scripta Materialia* **2013**, *68* (9), 723-726.
- 20. Mokhtari, M.; Le Bourlot, C.; Adrien, J.; Bonnin, A.; Wada, T.; Duchet-Rumeau, J.; Kato, H.; Maire, E., Microstructure characterization by X-ray tomography and EBSD of porous FeCr produced by liquid metal dealloying. *Materials Characterization* **2018**, *144*, 166-172.
- 21. Lu, Z.; Li, C.; Han, J.; Zhang, F.; Liu, P.; Wang, H.; Wang, Z.; Cheng, C.; Chen, L.; Hirata, A.; Fujita, T.; Erlebacher, J.; Chen, M., Three-dimensional bicontinuous nanoporous materials by vapor phase dealloying. *Nat Commun* **2018**, *9* (1), 276.
- 22. Han, J.; Li, C.; Lu, Z.; Wang, H.; Wang, Z.; Watanabe, K.; Chen, M., Vapor phase dealloying: A versatile approach for fabricating 3D porous materials. *Acta Materialia* **2019**, *163*, 161-

- 23. Yi Ding, J. E., Nanoporous Metals with Controlled Multimodal Pore Size Distribution. *J. AM. CHEM. SOC.* **2003**, *125*, 7772-7773.
- 24. Song, T.; Yan, M.; Shi, Z.; Atrens, A.; Qian, M., Creation of bimodal porous copper materials by an annealing-electrochemical dealloying approach. *Electrochimica Acta* **2015**, *164*, 288-296.
- 25. Snyder, J.; Asanithi, P.; Dalton, A. B.; Erlebacher, J., Stabilized Nanoporous Metals by Dealloying Ternary Alloy Precursors. *Advanced Materials* **2008**, *20* (24), 4883-4886.
- 26. Xu, J.; Zhang, C.; Wang, X.; Ji, H.; Zhao, C.; Wang, Y.; Zhang, Z., Fabrication of bimodal nanoporous bimetallic Pt–Au alloy with excellent electrocatalytic performance towards formic acid oxidation. *Green Chemistry* **2011**, *13* (7), 1914–1922.
- 27. Wang, X.; Sun, J.; Zhang, C.; Kou, T.; Zhang, Z., On the Microstructure, Chemical Composition, and Porosity Evolution of Nanoporous Alloy through Successive Dealloying of Ternary Al–Pd–Au Precursor. *The Journal of Physical Chemistry C* **2012**, *116* (24), 13271-13280.
- 28. Lu, Q.; Hutchings, G. S.; Yu, W.; Zhou, Y.; Forest, R. V.; Tao, R.; Rosen, J.; Yonemoto, B. T.; Cao, Z.; Zheng, H.; Xiao, J. Q.; Jiao, F.; Chen, J. G., Highly porous non-precious bimetallic electrocatalysts for efficient hydrogen evolution. *Nat Commun* **2015**, *6*, 6567.
- 29. Qiu, H.; Dong, X.; Huang, X., Design of nanoporous metals with bimodal pore size distributions for enhanced biosensing. *Nanoscale* **2012**, *4* (15), 4492-7.
- 30. Pham, Q. N.; Shao, B.; Kim, Y.; Won, Y., Hierarchical and Well-Ordered Porous Copper for Liquid Transport Properties Control. *ACS Appl Mater Interfaces* **2018**, *10* (18), 16015-16023.
- 31. Luo, Z.; Xu, J.; Yuan, B.; Hu, R.; Yang, L.; Gao, Y.; Zhu, M., 3D Hierarchical Porous

- Cu-Based Composite Current Collector with Enhanced Ligaments for Notably Improved Cycle Stability of Sn Anode in Li-Ion Batteries. *ACS Appl Mater Interfaces* **2018**, *10* (26), 22050-22058.
- 32. Zhang, S.; Xing, Y.; Jiang, T.; Du, Z.; Li, F.; He, L.; Liu, W., A three-dimensional tin-coated nanoporous copper for lithium-ion battery anodes. *Journal of Power Sources* **2011**, *196* (16), 6915-6919.
- 33. Song, R.; Zhang, L.; Zhu, F.; Li, W.; Fu, Z.; Chen, B.; Chen, M.; Zeng, H.; Pan, D., Hierarchical Nanoporous Copper Fabricated by One-Step Dealloying Toward Ultrasensitive Surface-Enhanced Raman Sensing. *Advanced Materials Interfaces* **2018**, *5* (16), 1800332.
- 34. Zhang, H.; Pan, Q.; Zhang, H., Multi-scale porous copper foams as wick structures. *Materials Letters* **2013**, *106*, 360-362.
- 35. Heon-Cheol Shin; Liu, M., Copper Foam Structures with Highly Porous Nanostructured Walls. *Chem. Mater.* **2004**, *16*, 5460-5464.
- 36. Huan Liu; Errui Wang; Qi Zhang; Yibin Renb; Xianwei Guo; Lin Wang; Guangyin Li; Yu, H., Unique 3D nanoporous/macroporous structure Cu current collector for dendrite-free lithium deposition. *Energy Storage Materials* **2019**, *17*, 253-259.
- 37. Zou, L.; Ge, M.; Zhao, C.; Meng, Q.; Wang, H.; Liu, X.; Lin, C. H.; Xiao, X.; Lee, W. K.; Shen, Q.; Chen, F.; Chen-Wiegart, Y. K., Designing Multiscale Porous Metal by Simple Dealloying with 3D Morphological Evolution Mechanism Revealed via X-ray Nano-tomography. *ACS Appl Mater Interfaces* **2020**, *12*, 2793–2804.
- 38. Lobanov, S. S.; Daly, J. A.; Goncharov, A. F.; Chan, X.; Ghose, S. K.; Zhong, H.; Ehm, L.; Kim, T.; Parise, J. B., Iodine in Metal-Organic Frameworks at High Pressure. *J Phys Chem A* 2018, *122* (29), 6109-6117.

- 39. Duan, Y.; Yang, L.; Zhang, M.-J.; Chen, Z.; Bai, J.; Amine, K.; Pan, F.; Wang, F., Insights into Li/Ni ordering and surface reconstruction during synthesis of Ni-rich layered oxides. *Journal of Materials Chemistry A* **2019**, *7* (2), 513-519.
- 40. Chen-Wiegart, Y. C.; Camino, F. E.; Wang, J., Sample preparation of energy materials for X-ray nanotomography with micromanipulation. *Chemphyschem* **2014**, *15* (8), 1587-91.
- 41. Ge, M.; Coburn, D. S.; Nazaretski, E.; Xu, W.; Gofron, K.; Xu, H.; Yin, Z.; Lee, W.-K., One-minute nano-tomography using hard X-ray full-field transmission microscope. *Applied Physics Letters* **2018**, *113* (8), 083109.
- 42. Gursoy, D.; De Carlo, F.; Xiao, X.; Jacobsen, C., TomoPy: a framework for the analysis of synchrotron tomographic data. *J Synchrotron Radiat* **2014**, *21*, 1188-1193.
- 43. O'Mara, A.; King, A. E.; Vickers, J. C.; Kirkcaldie, M. T. K., ImageSURF: An ImageJ Plugin for Batch Pixel-Based Image Segmentation Using Random Forests. *Journal of Open Research Software* **2017**, *5* (17), 31.
- 44. Collins, J. M.; King, A. E.; Woodhouse, A.; Kirkcaldie, M.; Vickers, J., Age moderates the effects of traumatic brain injury on beta-amyloid plaque load in APP/PS1 mice. *J Neurotrauma* **2019**, 36 (11), 1876-1889.
- 45. Chen-Wiegart, Y.-c. K.; DeMike, R.; Erdonmez, C.; Thornton, K.; Barnett, S. A.; Wang, J., Tortuosity characterization of 3D microstructure at nano-scale for energy storage and conversion materials. *Journal of Power Sources* **2014**, *249*, 349-356.
- 46. Münch, B.; Holzer, L., Contradicting Geometrical Concepts in Pore Size Analysis Attained with Electron Microscopy and Mercury Intrusion. *Journal of the American Ceramic Society* **2008**, *91* (12), 4059-4067.

- 47. Bae, C. J.; Erdonmez, C. K.; Halloran, J. W.; Chiang, Y. M., Design of battery electrodes with dual-scale porosity to minimize tortuosity and maximize performance. *Adv Mater* **2013**, *25* (9), 1254-8.
- 48. Erlebacher, J.; Aziz, M. J.; Karma, A.; Dimitrov, N.; Sieradzki, K., Evolution of nanoporosity in dealloying. *Nature* **2001**, *410* (6827), 450-3.
- 49. Chang-Jun Bae; Can K. Erdonmez; John W. Halloran; Chiang, Y.-M., Design of Battery Electrodes with Dual-Scale Porosity to Minimize Tortuosity and Maximize Performance. *Adv. Mater.* **2013**, *25*, 1254–1258.